Stress Controlled Rheology of Dense Suspensions Using Transient Flows

Endao Han, Nicole M. James, and Heinrich M. Jaeger

Phys. Rev. Lett. **123**, 248002 — Published 9 December 2019

DOI: 10.1103/PhysRevLett.123.248002

Stress controlled rheology of dense suspensions using transient flows

Endao Han,[1,2,*] Nicole M. James,[1,3] and Heinrich M. Jaeger[1,2]

[1] *James Franck Institute, The University of Chicago, Chicago, Illinois 60637, USA*
[2] *Department of Physics, The University of Chicago, Chicago, Illinois 60637, USA*
[3] *Department of Chemistry, The University of Chicago, Chicago, Illinois 60637, USA*

(Dated: November 14, 2019)

Dense suspensions of hard particles in a Newtonian liquid can be jammed by shear when the applied stress exceeds a certain threshold. However, this jamming transition from a fluid into a solidified state cannot be probed with conventional steady-state rheology because the stress distribution inside the material cannot be controlled with sufficient precision. Here we introduce and validate a method that overcomes this obstacle. Rapidly propagating shear fronts are generated and used to establish well-controlled local stress conditions that sweep across the material. Exploiting such transient flows, we can track how a dense suspension approaches its shear jammed state dynamically, and quantitatively map out the onset stress for solidification in a state diagram.

Suspending solid particles in a liquid creates a more viscous fluid [1–3]. For sufficiently large volume fraction ϕ of particles, the suspension becomes non-Newtonian, and the viscosity depends on the shearing intensity. Non-Newtonian behaviors commonly include continuous shear thickening (CST) [4–6], where the viscosity increases mildly with applied shear and, for larger ϕ, discontinuous shear thickening (DST) [7–9], where the viscosity can increase by more than an order of magnitude. Even richer dynamics occur when ϕ approaches the threshold for jamming [10, 11]: at sufficiently high shear stress, suspensions can reversibly transform from a viscous fluid into a solidified state [12, 13]. Experiments [9, 14–19] and simulations [20, 21] both suggest that strong thickening and solidification due to shear are related to a stress-dependent change in particle-particle interactions, which switch from lubrication at low stress to direct, frictional contact at high stress. A phenomenological model that unifies CST and DST within a framework based on such stress-dependent interactions was developed by Wyart and Cates [22]. Predictions of this model for the shear thickening regime have been validated by experimental [17, 23, 24] and numerical [21, 25–27] work. Importantly, the model also makes predictions for the transition into the shear jammed, solid-like state but these have not yet been tested.

A key reason for this is that a direct test requires conditions in which the local shear stress can be controlled. By contrast, conventional experiments, as well as simulations, control the shear rate or the shear stress only at the boundaries of a suspension, which means that unsteady flow can develop in the interior and local stress control is lost, a situation especially likely during DST or when the suspension is about to transform into a solid [23, 28].

It turns out, however, that a different means of applying shear can establish a local environment that is stress controlled. This is the transient process of stress-activated solidification, which has been studied under conditions of impact [12, 29–31], extension [32, 33], or simple shear [13, 34]. In each case, rapid external forcing turns the suspension into a jammed

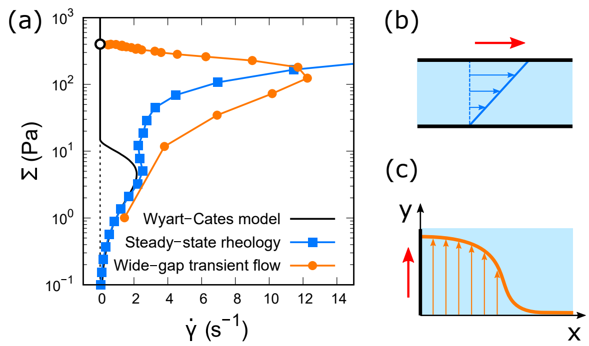

FIG. 1: (a) Relation between shear stress Σ and shear rate $\dot{\gamma}$ for a suspension in the SJ regime. Steady-state rheology was performed with parallel plates geometry schematically illustrated in (b), and the transient flow in a wide-gap geometry is shown in (c). Red arrows indicate the motions of the solid boundaries.

solid, which can "melt" and return to a fluid state once the applied stress is removed [12, 13, 35, 36]. The key element here is that this dynamic jamming, irrespective of how it is triggered, proceeds via propagating fronts that build up a region that sustains high stress between the front and the solid driving boundary. As these fronts penetrate the material, they therefore create local stresses that are, in turn, controlled by the forcing applied at the boundary [34].

Here we show how propagating fronts can be exploited to perform stress-controlled rheology in regimes inaccessible to methods based on steady-state driving[1]. By generating quasi-one-dimensional fronts in a wide-gap shear geometry, we quantitatively test a major prediction of the Wyart-Cates model [22] for the location of the boundary delineating DST and shear-jammed states as a function of packing fraction and applied stress.

Under steady driving conditions, the state of a dense suspension with packing fraction ϕ can be described by two parameters: the shear stress Σ and the shear rate $\dot{\gamma}$. As an example, the black line in Fig. 1(a)

*E-mail:endao.han1988@gmail.com

[1] Here steady driving includes shearing with constant velocity or constant force at the boundary.

shows the flow curve predicted by the Wyart-Cates model [22] for a suspension in the shear jamming (SJ) regime under stress-controlled conditions. With increasing Σ it bends back towards low $\dot{\gamma}$, and eventually, intersects with the vertical axis where $\dot{\gamma} = 0$ s^{-1}. At that intersection, the suspension can sustain non-zero shear stress at zero shear rate, and therefore must have developed a finite, non-zero shear modulus. This means the suspension is now jammed. We call the stress at this point the onset stress of shear jamming, $\Sigma_{\rm SJ}$. As increasing shear stress is applied, the jammed suspension remains solid (vertical portion of the black line along the vertical axis) until Σ eventually exceeds the yield stress of the jammed solid (not shown).

However, when this model is compared to steady-state experimental data (blue squares in Fig. 1(a)), we see apparent deviations. The data were taken with a cornstarch suspension of $\phi = 0.52$ [37, 38], using a parallel-plate geometry (Fig. 1(b)) under stress-controlled shearing conditions. Here ϕ was well above the frictional jamming packing fraction $\phi_{\rm m} = 0.45$ [34], which is the lower limit that allows SJ. As the figure shows, though the model does a good job predicting the results at $\Sigma < 5$ Pa, the measured Σ-$\dot{\gamma}$ curve bends only slightly towards low $\dot{\gamma}$ at high Σ. Instead of intersecting with the $\dot{\gamma} = 0$ s^{-1} axis as expected for SJ, the curve eventually bends forward again. Such behavior is typical for DST, a regime in which the Wyart-Cartes model predicts s-shaped Σ-$\dot{\gamma}$ curves [17, 22, 24]. The question thus arises: what causes these deviations from the model?

Rheology experiments can be performed with a variety of geometries. The most common geometries are parallel plates, cone and plate, and concentric cylinders (Couette cell). For all three geometries, the basic idea is similar: the sample is placed inside a narrow gap (normally 0.1-1 mm) and sheared continuously. To obtain the correct viscosity from such measurements, certain conditions must hold: the flow must be steady such that $\partial \mathbf{u}/\partial t = 0$; $\dot{\gamma}$ and Σ in the bulk must have well-defined spatial profiles so they can be calculated from the boundary conditions; and there is no boundary slip. Based on recent work on unsteady phenomena, when Σ exceeds the onset stress of DST, $\Sigma_{\rm DST}$, there can be complex spatial and temporal rate fluctuations even though the average stress at the boundary is held constant [23, 28, 40, 41] and, in addition, boundary slip can be significant [13, 28, 39, 42]. As a result, it is exceedingly difficult to maintain a uniformly sheared jammed state under steady-state driving or to even approach a jammed state in a truly stress-controlled manner with typical, narrow-gap rheology experiments.

However, there is another, experimentally accessible path to jamming by shear, as shown in Fig. 1(a). Instead of moving up along the black curve, we can get toward shear-jammed states (such as, e.g., the state indicated by the open black circle) as asymptotic limits of specific Σ-$\dot{\gamma}$ paths like the one indicated by the orange circles. These data were taken with the same suspension, but using a wide-gap shear configuration shown in Fig. 1(c). Note how this curve bends back strongly and can get much closer to the vertical axis than the blue data. We now describe how such flow curves can be used to perform rheology measurements.

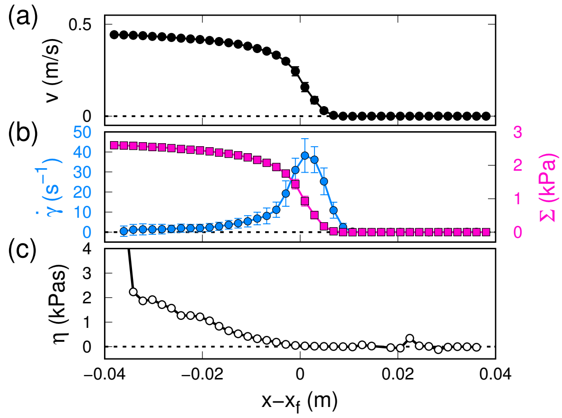

FIG. 2: Front profiles in the co-moving frame for a suspension with $\phi = 0.53$. (a) Velocity profile $v(x - x_{\rm f})$. (b) Shear stress Σ (magenta squares) and shear rate $\dot{\gamma}$ (blue circles) profiles. (c) Local viscosity $\eta = \Sigma/\dot{\gamma}$.

In our wide-gap shear configuration, a 1 cm thick, horizontal layer of suspension was floated on heavy oil, and a straight vertical plate in the suspension was used as the solid boundary that applied the shear [43]. Fig. 1(c) sketches the top view of the system. The left boundary moves with a constant speed U_0 along the y-direction. Immediately after start-up, a transient flow develops in the x-direction, perpendicular to the movement of the boundary, and spreads across the initially quiescent suspension. For suspensions with $\phi > \phi_{\rm m}$, this flow generates a shear jamming front when U_0 is sufficiently fast, i.e., the applied stress sufficiently large [34, 44]. The profile of such fronts has an approximately invariant shape, thus it can be represented as

$$F(x,t) = F(x - U_{\rm f} t), \tag{1}$$

where F can be Σ, $\dot{\gamma}$, or the y component of the velocity v. We define the front position $x_{\rm f}$ as where $v = 0.45U_0$, which is also approximately where $\dot{\gamma}$ peaks. The front propagates with a constant speed $U_{\rm f} \equiv kU_0$, where k is the dimensionless front propagation speed. With increasing U_0, k reaches a maximum plateau or peak value $k_{\rm p}$ that increases with ϕ but becomes independent of U_0 [34].

To use the fronts for rheology, we need to know the local shear rate and stress generated by them. Given our effectively 1D flow, the equation of motion is

$$\rho \frac{\partial v}{\partial t} = -\frac{\partial \Sigma}{\partial x}, \tag{2}$$

which reflects the fact that the viscous stress is always balanced by the acceleration of the suspension. This allows us to obtain the local shear stress without measuring forces, simply by calculating the stress needed for the suspension to accelerate. From Eq. 1 and Eq. 2, we obtain $\Sigma = \rho U_{\rm f} v$, and therefore $\Sigma(x,t)$ has the same shape as $v(x,t)$, but with a prefactor $\rho U_{\rm f}$. The mean velocity profile $v(x - x_{\rm f})$ is shown in Fig. 2(a).

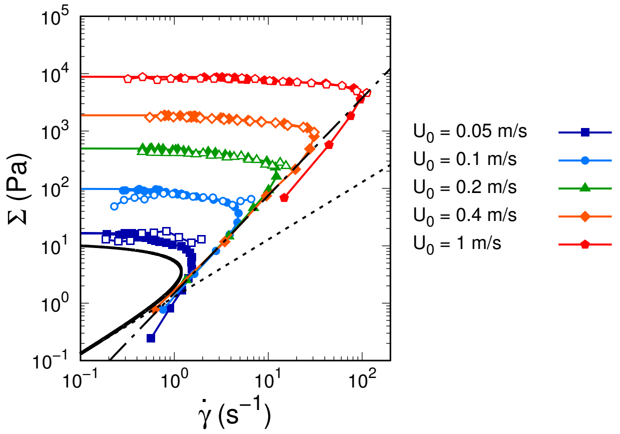

FIG. 3: Σ-$\dot{\gamma}$ flow curves for a suspension with $\phi = 0.53$, driven at different boundary speeds U_0. The solid black curve shows the prediction of the Wyart-Cates model. The dashed black line shows $\Sigma = \eta_{\rm N}\dot{\gamma}$. The dash-dot black line is $\Sigma \propto \dot{\gamma}^{1.7}$.

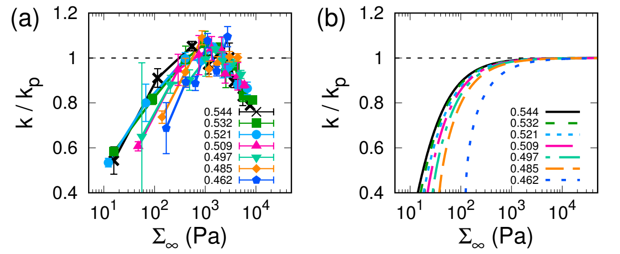

FIG. 4: (a)Normalized front propagation speed $k/k_{\rm p}$ as a function of shear stress Σ_∞ for different packing fractions ϕ. (b) Predictions of the generalized Wyart-Cates model (Eq. 5).

Here $v(x,t)$ was shifted by $x_{\rm f}$ and then averaged to obtain $v(x - x_{\rm f})$. The corresponding shear stress is shown in Fig. 2(b). As $(x - U_{\rm f}t) \to -\infty$, $v \to U_0$, and Σ asymptotically approaches $\Sigma_\infty = \rho k U_0^2$. Since this stress originates from the acceleration of the whole flow, which develops with little variation in shape before the front reaches a solid boundary, Σ_∞ is very stable.

The local shear rate $\dot{\gamma} = |\partial v/\partial x|$ calculated from the averaged velocity profile is also shown in Fig. 2(b). Because ours is a 1D system, we take $\dot{\gamma}$ to be positive for simplicity. We can see that both Σ and $\dot{\gamma}$ increase at the leading edge of the front ($x > x_{\rm f}$). However, behind the front ($x < x_{\rm f}$), Σ keeps increasing and approaches Σ_∞, while $\dot{\gamma}$ decreases and approaches zero. This means that the viscosity $\eta = \Sigma/\dot{\gamma}$ increases dramatically behind the front, as shown in Fig. 2(c).

Moreover, compared to DST, where $\eta \propto \Sigma$, the viscosity increase here is "beyond discontinuous", because now η diverges as $\Sigma \to \Sigma_\infty$ (see Suppl. Mat.). In other words, once the front passes, the suspension will evolve toward a solid-like shear-jammed state with finite shear modulus so that $\dot{\gamma}|_{t\to+\infty} \to 0$.

While we plot the orange curve in Fig. 1(a) together with the steady-state prediction and experiment, this transient flow curve needs to be interpreted differently. For any point on a steady-state flow curve, the overall accumulated strain $\gamma = \int \dot{\gamma} dt$ is irrelevant since the curve describes a stationary state. In contrast, under transient conditions, the state of the suspension evolves with time, and each point on the Σ-$\dot{\gamma}$ curve corresponds to a different γ. For example, the orange curve in Fig. 1(a) starts from $\gamma = 0$ at small Σ. In accordance with Fig. 2(b), as γ accumulates while the front sweeps through, Σ and $\dot{\gamma}$ both increase following a power law (Fig. 3) until $\dot{\gamma}$ reaches its maximum and then decreases toward zero. Since the front propagates with a constant speed, $\gamma(x,t)$ is always proportional to $v(x,t)$, and thus $\Sigma(x,t)$, during the process (see Suppl. Mat. for details).

Importantly, the specific stress level Σ_∞ that is approached in this manner within the range of jammed states is fully controlled by U_0, as shown in Fig. 3. The data here were obtained by two analysis methods. Solid points are from the mean velocity profiles $v(x - x_{\rm f})$, and Σ and $\dot{\gamma}$ were extracted the same way as in Fig. 2. Open circles were obtained by first calculating Σ and $\dot{\gamma}$ from the velocity profiles at each time step, and then averaging Σ and $\dot{\gamma}$. The two methods match well, especially at large U_0. This technique enables us to systematically probe the theoretical onset boundary of SJ (black curve in Fig. 3) and the corresponding $\Sigma_{\rm SJ}$, because when a smaller stress is applied, jamming fronts can not be generated and the Σ-$\dot{\gamma}$ curves will be qualitatively different from those shown in Fig. 3.

To be more quantitative, we not only find the conditions under which a jamming front is observed but also can extract its dimensionless front speed k as a function of Σ_∞, as shown in Fig. 4(a). In the SJ regime, since $\dot{\gamma} \to 0\ {\rm s}^{-1}$ eventually, γ approaches a finite value γ_∞ asymptotically. The dimensionless front propagation speed is directly controlled by this asymptotic strain, as $k = 1/\gamma_\infty$ [34]. Since γ_∞ is a function of ϕ, so is k. For suspensions prepared with different ϕ, we normalized $k(\phi)$ by its mean peak height, $k_{\rm p}(\phi)$. In general, $k/k_{\rm p}$ grows from 0 to 1 as Σ_∞ increases, with suspensions at smaller ϕ requiring larger stress Σ_∞ to reach the same $k/k_{\rm p}$.

Now we compare the experimental measurements with the generalized Wyart-Cates model [34], in which the constitutive relation is written as

$$\Sigma = \eta_0 \dot{\gamma} \left[1 - \frac{\phi}{\phi_0 - f(\Sigma) g(\gamma)(\phi_0 - \phi_{\rm m})} \right]^{-2}, \qquad (3)$$

where η_0 is the solvent viscosity and ϕ_0 is the frictionless jamming packing fraction. As long as f and g are continuous monotonic functions that satisfy $f(0) = g(0) = 0$ and $f(+\infty) = g(+\infty) = 1$, the model works qualitatively. For the suspensions that we use, $g(\gamma) = 1 - \exp(-\gamma/\gamma^*)$ agrees well with experimental results [34]. The form of $f(\Sigma)$, on the other hand, has been proposed in various forms [22, 40, 46, 47]. Here we use $f(\Sigma) = \exp(-\Sigma^*/\Sigma)$ [46, 47]. In the equations, γ^* and Σ^* are the characteristic strain and stress scales, respectively. The behavior of steady-state rheology is recovered in the $\gamma \to \infty$ limit where

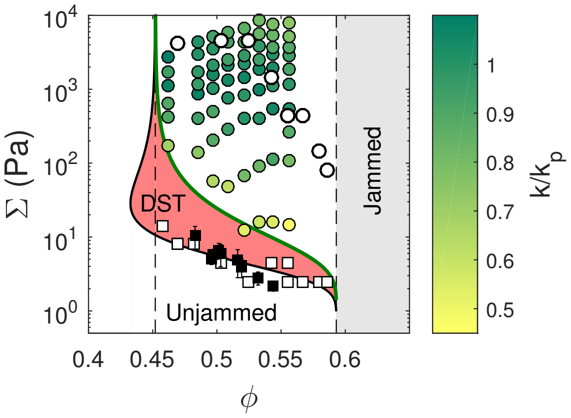

FIG. 5: State diagram. Squares are the onset stress of DST obtained from standard rheology with parallel plates (black) [34] and wide-gap Couette cell (open) [13]. Solid circles show the SJ regime mapped out by our experiments with transient flows ($\Sigma_\infty(\phi)$). Open circles are the onset stress of SJ from Peters *et al.* [13]. The red region shows the DST regime and the green curve shows Σ_{SJ} (Eq. 6) predicted by the Wyart-Cates model [22].

$g(\gamma) \to 1$, such as the black curves in Fig. 1 and Fig. 3.

The suspension reaches a shear jammed state when the terms in the square bracket in Eq. 3 vanish (see Suppl. Mat.). As a result, we have

$$f(\Sigma_\infty)g(\gamma_\infty) = \frac{\phi_0 - \phi}{\phi_0 - \phi_{\mathrm{m}}} \equiv 1 - \Phi, \tag{4}$$

and thus $\gamma_\infty(\Sigma_\infty) = g^{-1}\left[(1-\Phi)/f(\Sigma_\infty)\right]$, where Φ is a rescaled packing fraction and g^{-1} is the inverse function of g. In the high stress limit where $\Sigma_\infty \gg \Sigma^*$, $f(\Sigma_\infty) = 1$, thus $\gamma_\infty(\Sigma_\infty \gg \Sigma^*) = g^{-1}(1-\Phi)$, which corresponds to $1/k_{\mathrm{p}}$. Finally, we get the relationship between k/k_{p} and Σ_∞

$$\frac{k}{k_{\mathrm{p}}} = \frac{1/\gamma_\infty(\Sigma)}{1/\gamma_\infty(\Sigma \gg \Sigma^*)} = \frac{g^{-1}(1-\Phi)}{g^{-1}[(1-\Phi)/f(\Sigma_\infty)]}. \tag{5}$$

The results are presented in Fig. 4(b), and we see the stress dependence of k in agreement with the experiments. Note that in the experiments, at stresses above approximately 2,000 Pa, k/k_{p} deviates from 1 and decreases. We suspect that this is due to excessive dilatency of the system in the direction perpendicular to the x-y plane shown in Fig. 1(c), which was not confined in our experiments. In the model, we assume that ϕ is a constant, so any effect due to ϕ variation is not captured.

The agreement between the experiments and the model allows us to map out the boundary of the SJ regime in the state diagram, as shown in Fig. 5. From steady-state rheology experiments, we obtained ϕ_{m}, ϕ_0, and Σ^* [34]. The solid black curve shows Σ_{DST} calculated based on the Wyart-Cates model. Experimental measurements from steady-state rheology lie right on top of this predicted boundary. As expected, SJ is observed only when ϕ is between ϕ_{m} (left) and ϕ_0 (right) labeled by the vertical dashed lines. The predicted Σ_{SJ} is obtained by setting $g(\gamma) = 1$ in Eq. 4, thus

$$\Sigma_{\mathrm{SJ}} = -\frac{\Sigma^*}{\ln(1-\Phi)}. \tag{6}$$

This is shown by the solid green curve in Fig. 5, which our experiments now can test quantitatively. In a previous experiment by Peters *et al.*, a boundary for the SJ onset was obtained by observing whether a small sphere dropped onto the suspension remained on its surface or sank in [13]. This boundary is shown in Fig. 5 by the open circles. As we can see, it lies significantly above what the model predicts. In comparison, our experimental method more sensitively detects possible shear jammed states at relatively low stress. The solid circles in Fig. 5 show the region where jamming fronts are observed, and their colors map out the corresponding k/k_{p}. Combining the results shown in Fig. 4 and Fig. 5, we find that the Wyart-Cates model provides a remarkably good prediction of the onset of both DST and SJ.

In conclusion, we show that conventional steady-state rheology has limitations when testing suspensions in the regime where shear jamming is approached. To obtain flow curves for suspensions in this regime, we introduce a method that takes advantage of transient shear fronts in a wide-gap linear shear cell. As the front propagates, the dense suspension behind the front evolves toward a shear jammed state, and the stress of this jammed state can be controlled by the speed of the shearing boundary. This makes it possible to map out the onset stress for shear jamming at different packing fractions. We find that the Wyart-Cates model and its generalization can predict this onset stress as well as the stress-dependent front propagation speed.

Acknowledgments

This project originated from a collaboration with Matthieu Wyart. We thank Ivo Peters for providing data and suggestions. We thank Abhinendra Singh for useful discussions. We would also like to acknowledge the referees for many helpful suggestions. This work was supported by the US Army Research Office through grant W911NF-16-1-0078, the Center for Hierarchical Materials Design (CHiMaD), and the UChicago MRSEC (NSF grant DMR-1420709).

[1] G. K. Batchelor. The effect of brownian motion on the bulk stress in a suspension of spherical particles. *J. Fluid Mech.*, 83(01):97, 1977.

[2] S. H. Maron and P. E. Pierce. Application of reeeyring generalized flow theory to suspensions of spherical particles. *J. Colloid Sci.*, 11:80–95, 1956.

[3] I. M. Krieger and T. J. Dougherty. A mechanism for non-newtonian flow in suspensions of rigid spheres. *Transactions of the Society of Rheology*, 3(1):137–152, 1959.

[4] N. J. Wagner and J. F. Brady. Shear thickening in colloidal dispersions. *Physics Today*, 62(10):27–32, 2009.

[5] J. F. Brady and G. Bossis. The rheology of concentrated suspensions of spheres in simple shear flow by numerical simulation. *J. Fluid Mech.*, 155:105, 1985.

[6] X. Cheng, J. H. McCoy, J. N. Israelachvili, and I. Cohen. Imaging the microscopic structure of shear thinning and thickening colloidal suspensions. *Science*, 333:1276–1279, 2011.

[7] H. A. Barnes. Shear-thickening ("dilatancy") in suspensions of nonaggregating solid particles dispersed in newtonian liquids. *J. Rheol.*, 33(2):329, 1989.

[8] E. Brown and H. M. Jaeger. Shear thickening in concentrated suspensions: phenomenology, mechanisms and relations to jamming. *Rep. Prog. Phys.*, 77(4):046602, 2014.

[9] Eric Brown and Heinrich M. Jaeger. The role of dilation and confining stresses in shear thickening of dense suspensions. *J. Rheol.*, 56(4):875, 2012.

[10] A. J. Liu and S. R. Nagel. Jamming is not just cool any more. *Nature*, 396(6706):21–22, 1998.

[11] D. Bi, J. Zhang, B. Chakraborty, and R. P. Behringer. Jamming by shear. *Nature*, 480(7377):355–8, 2011.

[12] S. R. Waitukaitis and H. M. Jaeger. Impact-activated solidification of dense suspensions via dynamic jamming fronts. *Nature*, 487(7406):205–9, 2012.

[13] I. R. Peters, S. Majumdar, and H. M. Jaeger. Direct observation of dynamic shear jamming in dense suspensions. *Nature*, 532(7598):214–217, 2016.

[14] Q. Xu, S. Majumdar, E. Brown, and H. M. Jaeger. Shear thickening in highly viscous granular suspensions. *EPL*, 107(6):68004, 2014.

[15] N. Fernandez, R. Mani, D. Rinaldi, D. Kadau, M. Mosquet, H. Lombois-Burger, J. Cayer-Barrioz, H. J. Herrmann, N. D. Spencer, and L. Isa. Microscopic mechanism for shear thickening of non-brownian suspensions. *Phys. Rev. Lett.*, 111(10):108301, 2013.

[16] F. Boyer, E. Guazzelli, and O. Pouliquen. Unifying suspension and granular rheology. *Phys. Rev. Lett.*, 107(18):188301, 2011.

[17] B. M. Guy, M. Hermes, and W. C. Poon. Towards a unified description of the rheology of hard-particle suspensions. *Phys. Rev. Lett.*, 115(8):088304, 2015.

[18] J. Comtet, G. Chatte, A. Nigues, L. Bocquet, A. Siria, and A. Colin. Pairwise frictional profile between particles determines discontinuous shear thickening transition in non-colloidal suspensions. *Nat. Commun.*, 8:15633, 2017.

[19] Nicole M. James, Endao Han, Ricardo Arturo Lopez de la Cruz, Justin Jureller, and Heinrich M. Jaeger. Interparticle hydrogen bonding can elicit shear jamming in dense suspensions. *Nature Materials*, 17(11):965–970, 2018.

[20] R. Seto, R. Mari, J. F. Morris, and M. M. Denn. Discontinuous shear thickening of frictional hard-sphere suspensions. *Phys. Rev. Lett.*, 111(21):218301, 2013.

[21] R. Mari, R. Seto, J. F. Morris, and M. M. Denn. Shear thickening, frictionless and frictional rheologies in non-brownian suspensions. *J. Rheol.*, 58(6):1693–1724, 2014.

[22] M. Wyart and M. E. Cates. Discontinuous shear thickening without inertia in dense non-brownian suspensions. *Phys. Rev. Lett.*, 112(9):098302, 2014.

[23] M. Hermes, B. M. Guy, W. C. K. Poon, G. Poy, M. E. Cates, and M. Wyart. Unsteady flow and particle migration in dense, non-brownian suspensions. *J. Rheol.*, 60(5):905–916, 2016.

[24] Z. Pan, H. de Cagny, B. Weber, and D. Bonn. S-shaped flow curves of shear thickening suspensions: direct observation of frictional rheology. *Phys. Rev. E*, 92(3):032202, 2015.

[25] R. Mari, R. Seto, J. F. Morris, and M. M. Denn. Nonmonotonic flow curves of shear thickening suspensions. *Phys. Rev. E*, 91(5):052302, 2015.

[26] C. Ness and J. Sun. Shear thickening regimes of dense non-brownian suspensions. *Soft Matter*, 12(3):914–924, 2016.

[27] A. Singh, R. Mari, M. M. Denn, and J. F. Morris. A constitutive model for simple shear of dense frictional suspensions. *J. Rheol.*, 62(2):457–468, 2018.

[28] Brice Saint-Michel, Thomas Gibaud, and Sbastien Manneville. Uncovering instabilities in the spatiotemporal dynamics of a shear-thickening cornstarch suspension. *Phys. Rev. X*, 8(3), 2018.

[29] M. Roche, E. Myftiu, M. C. Johnston, P. Kim, and H. A. Stone. Dynamic fracture of nonglassy suspensions. *Phys. Rev. Lett.*, 110(14):148304, 2013.

[30] E. Han, I. R. Peters, and H. M. Jaeger. High-speed ultrasound imaging in dense suspensions reveals impact-activated solidification due to dynamic shear jamming. *Nat. Commun.*, 7:12243, 2016.

[31] R. Maharjan, S. Mukhopadhyay, B. Allen, T. Storz, and E. Brown. Constitutive relation for the system-spanning dynamically jammed region in response to impact of cornstarch and water suspensions. *Phys. Rev. E*, 97(5), 2018.

[32] M. I. Smith, R. Besseling, M. E. Cates, and V. Bertola. Dilatancy in the flow and fracture of stretched colloidal suspensions. *Nat. Commun.*, 1:114, 2010.

[33] S. Majumdar, I. R. Peters, E. Han, and H. M. Jaeger. Dynamic shear jamming under extension in dense granular suspensions. *Phys. Rev. E*, 95:012603, 2017.

[34] Endao Han, Matthieu Wyart, Ivo R. Peters, and Heinrich M. Jaeger. Shear fronts in shear-thickening suspensions. *Phys. Rev. Fluids*, 3:073301, Jul 2018.

[35] Bin Liu, Michael Shelley, and Jun Zhang. Focused force transmission through an aqueous suspension of granules. *Phys. Rev. Lett.*, 105(18):188301, 2010.

[36] Stefan von Kann, Jacco H. Snoeijer, Detlef Lohse, and Devaraj van der Meer. Nonmonotonic settling of a sphere in a cornstarch suspension. *Phys. Rev. E*, 84(6):060401, 2011.

[37] See Supplemental Material for the formula and preparation of the suspensions. The parameters used in the Wyart-Cates model are measured experimentally with the same suspensions. Details of these measurements are shown in Ref. 33.

[38] Endao Han, Nigel Van Ha, and Heinrich M. Jaeger. Measuring the porosity and compressibility of liquid-suspended porous particles using ultrasound. *Soft Matter*, 13(19):3506–3513, 2017.

[39] S. Manneville, L. Bécu, and A. Colin. High-frequency ultrasonic speckle velocimetry in sheared complex fluids. *Eur. Phys. J. Appl. Phys.*, 28(3):361–373, 2004.

[40] H. Nakanishi, S. Nagahiro, and N. Mitarai. Fluid dynamics of dilatant fluids. *Phys. Rev. E*, 85(1):011401, 2012.

[41] V. Rathee, D. L. Blair, and J. S. Urbach. Localized stress fluctuations drive shear thickening in dense suspensions. *Proc. Natl. Acad. Sci. U.S.A.*, 114(33):8740–8745, 2017.

[42] W. H. Boersma, P. J. M. Baets, J. Laven, and H. N.

Stein. Time-dependent behavior and wall slip in concentrated shear thickening dispersions. *J. Rheol.*, 35(6):1093–1120, 1991.

[43] See Supplemental Material for a more detailed illustration of the experimental setup.

[44] See Supplemental Material for details on the flow under low stress and high stress in this wide-gap linear shear geometry, which includes Ref. [45].

[45] D. J. Acheson, *Elementary Fluid Dynamics*, Oxford University Press (2005).

[46] Abhinendra Singh, Romain Mari, Morton M. Denn, and Jeffrey F. Morris. A constitutive model for simple shear of dense frictional suspensions. *Journal of Rheology*, 62(2):457–468, 2018.

[47] R. N. Chacko, R. Mari, M. E. Cates, and S. M. Fielding. Dynamic vorticity banding in discontinuously shear thickening suspensions. *Phys. Rev. Lett.*, 121(10):108003, 2018.